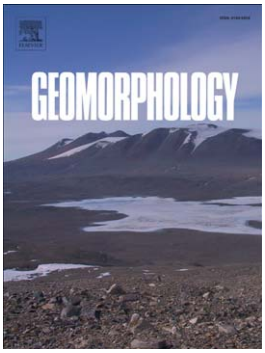

Impact of wind erosion on detecting active tectonics from geomorphic indexes in extremely arid areas: a case study from the Hero Range, Qaidam Basin, NW China

Lei Wu, Ancheng Xiao, Shufeng Yang

PII: S0169-555X(14)00357-2
DOI: doi: 10.1016/j.geomorph.2014.07.010
Reference: GEOMOR 4844

To appear in: *Geomorphology*

Received date: 15 September 2013
Revised date: 16 June 2014
Accepted date: 4 July 2014

Please cite this article as: Wu, Lei, Xiao, Ancheng, Yang, Shufeng, Impact of wind erosion on detecting active tectonics from geomorphic indexes in extremely arid areas: a case study from the Hero Range, Qaidam Basin, NW China, *Geomorphology* (2014), doi: 10.1016/j.geomorph.2014.07.010

Impact of wind erosion on detecting active tectonics from geomorphic indexes in extremely arid areas: a case study from the Hero Range, Qaidam Basin, NW China

Lei Wu [a, b], Ancheng Xiao[a*], and Shufeng Yang[a]

[a] *Department of Earth Sciences, Zhejiang University, Hangzhou 310027, China*

[b] *Department of Geology, University of California, Davis 95616, California, USA*

*Corresponding author.

Emails: wulei@zju.edu.cn (L. Wu), xiaoanch@zju.edu.cn (A. Xiao),

yjsy-ysf@zju.edu.cn (S. Yang)

Abstract: Geomorphologic analysis has been used widely to detect active tectonics in regions where fluvial incision is the major erosional process. In this paper, however, we assess the feasibility of utilizing these frequently-used geomorphic indexes (e.g., hypsometric curves, longitudinal channel profiles, normalized stream length-gradient (*SLK*) index) to determine active tectonics in extremely arid areas where wind erosion also plays an important role. The case study is developed on the Hero Range in the western Qaidam Basin, one of the driest regions on Earth with severe wind erosion since late Pliocene. The result shows that in the west and south sectors, as well as the western part of the east sector, of the Hero Range where fluvial incision prevails, these geomorphic indexes are good indicators of active faulting and consistent with the geological result based on study of fault traces, scarps, faulted Holocene fans and

historical seismicity within the past four decades. In contrast, along the northeastern margin (the NE and the SE parts of the east sector) of the range where wind erosion is also important, the results from the geomorphic indexes show quite active tectonics, contrary with the geological evidence favoring weakly active tectonics. Moreover, the positive *SLK* anomaly lies oblique to the fault trace and the anticline axis but parallel to the wind direction. To reconcile the contradiction, we propose that wind erosion caused by northwestern winds has a tendency to make geomorphic indexes exhibit anomalous values that indicate higher activities, by way of (1) lowering the base-level to generate knickpoints on the longitudinal channel profiles and therefore positive *SLK* anomalies, and (2) lateral erosion of the mountain front making the hypsometric curves and even the longitudinal channel profiles more convex, and producing obvious slope breaks.

Key words: Qaidam Basin; wind erosion; Hypsometric curves; stream length-gradient index; drainage analysis

1. Introduction

Present-day topography is a function of rock uplift, erosion and deposition (England and Molnar, 1990; Bishop, 2007; Burbank and Anderson, 2012), suggesting that geomorphic features are good indicators for active tectonics and surface processes. Owing to the increasingly easier acquisition of high-resolution DEM and remote sensing data, a growing number of achievements on geomorphological

response to active faulting and folding have been made over the past three decades (Seeber and Gornitz, 1983; Avouac and Peltzer, 1993; Jackson et al., 1996; Keller et al., 2000; Garcia and Herail, 2005; Pérez-Peña et al., 2010; Gao et al., 2013), giving us a good understanding of active tectonics in not only remote areas (Avouac and Peltzer, 1993; Clark et al., 2004) but also regions covered by Quaternary deposits without any obvious clues in the field (Keller et al., 2000; Hilley and Arrowsmith, 2008; Melosh and Keller, 2013).

A number of geomorphic indexes (e.g., stream length-gradient index, hypsometric curves, channel concavity and steepness) have proved to be good proxies for active faulting and folding in many active regions such as Himalaya and eastern Tibet (Kirby et al., 2003; Malik and Mohanty, 2007; Gao et al., 2013), Taiwan (Chen et al., 2003), the Betic Cordillera (Pedrera et al., 2009; Pérez-Peña et al., 2010; Azanon et al., 2012), the northern Apennine orogenic belt (Troiani and Della Seta, 2008) and the Transverse ranges in California (DiBiase et al., 2010). Most of the above-studied areas are regions where river incision is the major erosional process. It remains unknown whether these indexes are feasible to detect active tectonics in extremely arid areas, where annual precipitation is less than 100 mm and the fluvial incision is not so effective. Besides, wind erosion plays an important role in shaping the topography in the extremely arid areas, and its influence on the above geomorphic indexes needs to be carefully evaluated.

This paper aims to testify the applicability of using geomorphic indexes (e.g., hypsometric curves and integrals, longitudinal channel profiles and stream

length-gradient index) to detect active tectonics in extremely arid areas, from the case study of the Hero Range in the western corner of the Qaidam Basin (Fig. 1), one of the driest deserts on Earth. We evaluate the influence of wind erosion on these indexes in that wind erosion is a conspicuous erosional process in most area of the western Qaidam Basin since late Pliocene (Kapp et al., 2011). Our results shows that the selected geomorphic indexes are suitable for detecting active faulting where channel incision is dominant; however, they present anomalous values indicating higher activities that are not supported by field evidence or tectonic structures in areas where wind erosion is also important.

2. Background geology

2.1. Geological setting of the Qaidam Basin and the Hero Range

The Qaidam Basin, with an area of ca. 120,000 km^2, is the largest sedimentary basin inside the Tibetan Plateau. It is now surrounded by the Qilian orogenic belt to the northeast, the East Kunlun – Qiman Tagh orogenic belt to the south-southwest, and the Altyn Tagh Fault, one of the largest active strike-slip faults on Earth, to the northwest (Fig. 1a). The basin developed on the Proterozoic – Paleozoic basement in early Jurassic (Chen et al., 2005; Wu et al., 2011) and was an internally drained basin since at least Oligocene. The Cenozoic sediments within the basin is up to 10,000m thick, and consist mainly of saline to hypersaline lacustrine mudstone and siltstone, together with some fluvial sandstone and conglomerate at the margins (Rieser et al., 2005; Yin et al., 2008; Wu et al., 2012a; Wu et al., 2012b). Strong crustal shortening

occurred inside the Qaidam Basin since middle – late Miocene (Liu et al., 2009; Zhang et al., 2013; Wu et al., 2014), forming lots of NW- to NWN-trending folds in its western part, with the Hero Range as one of the largest anticlinoria (Fig. 1b).

Most of the area inside the Qaidam Basin is of low topographic relief (< 100m) except the Hero Range. This NW-trending and ca. 30 km-wide intra-basin range is located in the western corner of the Qaidam Basin and stands as much as 800 m higher than adjacent regions (Figs. 1, 2, 3a). It is separated from the Pingding Shan double bend of the Altyn Tagh Fault system to the northwest by two north-dipping reverse faults (F1 and F2, Fig. 2), and extends ca. 200 km with decreasing altitude towards southeast (Figs. 1b, 3b). The main body of the northwestern half of the Hero Range, the study area in this paper, consists generally of five NW- to NWN-trending anticlines (Figs. 2, 4): the Xianshuiquan and the Youquanzi anticlines formed by a SW-dipping basement-involved reverse fault (F6) along the northeastern margin; the Shizigou and the Youshashan anticlines with steep or even overturned southwestern limbs that are controlled by NE-dipping Shizigou (F3) and Youshashan (F4) thrust faults along the southwestern margin; and the nearly symmetric, southeast-plunging Ganchaigou anticline along the central axis. Rocks exposed in the Hero Range are mostly middle Miocene – early Pliocene fluvio-lacustrine siltstones, mudstones and sandstones interbedded with few conglomerates. Paleocene – early Miocene sediments with similar rock types are only seen in the cores of anticlines (Fig. 1b).

The northwestern end of the Hero Range is constituted by three topographic highs corresponding to the Shizigou, the Ganchaigou and the Xianshuiquan anticlines

from southwest to northeast (Fig. 3c). As these highs merge together to the southeast, the correspondence between topographic and structural highs (cores of anticlines) no longer exists (Figs. 3d – 3f). This along-strike variation may result from two reasons. First, deformation was stronger and more localized in individual anticlines in the northwestern part but more distributed in the southeastern part, because the former is closer to the Altyn Tagh Fault (Fig. 2) on which slip has been regarded as the main driving force of the NE-SW-directed crustal shortening inside the Qaidam basin since the mid-Miocene (Wu et al., 2013). Secondly, headward erosion led to migration of channel sources towards the center of the Hero Range. The swath profiles across the Hero Range also reveal that the base-level of the southwestern side is ca. 120 m higher than that of the northeastern side (Fig. 3).

2.2. Wind erosion around the Hero Range

Qaidam Basin is one of the driest deserts on Earth. Annual precipitation is about 50 mm around the Hero Range but decreases to only ca. 16 mm near Lenghu, about 200 km to the east (data from the hydrographic stations in the Huatugou and the Lenghu towns, respectively, Fig.1b). Despite the dry weather, most of the Hero Range is still highly dissected by fluvial channels with channel incision up to 150 m (Figs. 5a – 5c).

The exposed Cenozoic rocks within the basin are mostly poorly-cemented lacustrine mudstone and siltstone (Kapp et al., 2011). Strong northwesterly winds entering the basin through topographic lows in the Altyn mountain erode these low-resistant rocks by deflation since the late Pliocene (Kapp et al., 2011), forming

lots of yardangs (Goudie, 2008) in areas to the northeast of the Hero Range. These eroded materials were transported eastward by winds and deposited on the Chinese Loess Plateau (Pullen et al., 2011). Our field mapping and remote sensing images show that the northeastern margin of the Hero Range is also highly eroded by winds, as evidenced by the presence of steep cliffs, yardangs and sand dunes (Figs. 5d – 5i). Landforms partly deflated by winds are also seen commonly (Fig. 5h).

Some isolated alluvial-fans, with fairly smooth surfaces that slope gently to the northeast, are found between the northeastern mountain front and the axis of the Youquanzi anticline (Figs. 5e, 5g, 5j). Below the fans, there exist some old yardangs forming prior to the deposition of the fans (Fig. 5k). The fans and old yardangs both stand several to tens of meters higher than the adjacent deformed Miocene fragile strata where plenty of young (modern) yardangs are developed, due possible to the higher resistance to wind erosion of the fans (Figs. 5j, 5k). We interpret that the fans were deposited between two wind-erosion events that formed old and young yardangs, respectively (Fig. 5k). This supports the simulation result of Kapp et al. (2011) that the Qaidam Basin was characterized by alternating strong wind erosion during glacial periods, and weak wind erosion and/or alluvial-fluvial deposition during interglacial period. Albeit lack of accurate dating data, we regard that these fans could form at least during the last interglacial period (110 – 130 ka before present) because there are few alluvial deposits nearby during the present interglacial period (Figs. 5d – 5j). Two additional meaningful inferences could also be obtained. First, the local base-level to the northeastern side of the Hero Range was

lowered by winds over time, as evidenced by the fact that these old fans, without any surrounding faults, were deposited to a base-level tens of meters higher than the present base-level (Fig. 5k). Secondly, the width of the Hero Range decreased over time by lateral wind erosion (Fig. 5k), as suggested by these fans now being 1-2 km away from the present-day mountain front, and the present-day northeastern mountain front being about 3 – 8 km southwest of the structural boundary defined by fault F6 (Figs. 3f, 4, 5d, 5e, 5h).

The above observations indicate that the present-day topography of the Hero Range is mainly the result of fluvial incision with influence of wind erosion along the northeastern margin. According to the proportions of channels, Yardangs and sand dunes, we subdivided the Hero Range and its adjacent area into three zones (Fig. 2): 1) a western zone dominated by fluvial incision with slight wind deflation and containing most area of the Hero Range, 2) a narrow central zone characterized by both fluvial incision and wind erosion along the northeastern margin of the Hero Range, and 3) an eastern zone dominated by wind erosion and playa deposition to the northeast of the Hero Range, which has already been studied by Kapp et al. (2011), Heermance et al. (2013) and Rohrmann et al. (2013) in detail.

3. Active tectonics in the Hero Range

Previous mapping on active tectonics shows that the Shizigou and the Youshashan faults (F3 and F4, Fig. 2), defining the southwestern edge of the Hero Range, are both active (Taylor and Yin, 2009), as evidenced by clear fault scarps and

traces (Figs. 6a, 6b). In the westernmost part of the Youshashan anticline, the Youshashan fault (F4) obviously cut and folded the alluvial fans at the front of the Hero Range (Figs. 6c, 6d). The age of these fans could be younger than 0.71 Ma according to the magnetostratigraphic dating on a sedimentary section about 25 km to the northwest (Zhang et al., 2013). Topographic profiles on the fan surfaces show that vertical offsets on the Youshashan fault (F4) generally decrease westward, with a maximum value of ~28.6 m (Fig. 6e). In the eastern flank of the Ganchaigou anticline, a SW-dipping fault named as the Gandong fault (F5) is evident (Figs. 2, 4), causing the strata in the hangingwall to be 35° - 60° steeper than those in the footwall (Fig. 6f). Although no clear active fault scarps are found along the fault F5, a cluster of channel merging and bending across the fault (Fig. 6g) indicates it may still be active. Despite that the SW-dipping fault F6 is explicit in the seismic profile (Fig. 4), the corresponding fault traces are not so evident in the field along the northeastern edge of the Hero Range. The possible scarps of fault F6 separating the Xianshuiquan and the Youquanzi anticlines to the southwest from the modern salt playas to the northeast are highly diffused and eroded, as shown by remote sensing images from the Google Earth (Figs. 6h, 6i), suggesting that the present-day activity on fault F6 may be fairly weak.

Instrumental records of historical seismicity with magnitude > Mw 2.0 (Fig. 2) indicate that natural earthquakes concentrated in the southern part of the Hero Range (Youshashan anticline) with the largest one (Mw 6.3) occurring on January 2nd 1977 on the Youshashan fault (F4) over the past 40 years (Fig. 2). One earthquake

with a magnitude of Mw 4.4 happened on the northern tip of the Shizigou fault (F3, Fig. 2). On the northeastern side of the Hero Range, only one earthquake with a magnitude of Mw 3.4 was recorded close to the southeastern tip of the Gandong fault (F5). No earthquake happened on fault F6 within the study area over the last four decades (Fig. 2).

Table 1 summaries the result of active tectonics in the Hero Range based on geological observations and historical seismicity. To quantify the intensity of fault activities, we assigned values of 1, 2 and 3 to the field evidence supporting weakly, moderately and strongly active tectonics, respectively (Table 1). The overall activity of each fault is then quantified by a geological activity index, which is defined as the mean value of the corresponding geological evidence for this fault (Table 1). We regard the activity index of >2.5, 1.5 – 2.5 and < 1.5 as indicators of strong, moderate, and weak activity, respectively (Table 1). The Shizigou (F3) and the Youshashan (F4) faults with geological activity indexes of 2.67 and 3, respectively, are strongly active, as evidenced by the occurrence of clear fault traces, scarps, faulted Holocene fans, and high frequency of seismicity. The Gandong fault (F5) in the eastern flank of the Ganchaigou anticline is deemed as being moderately active because the geological activity index is 2 based on the clear fault trace in the field, the existence of limited historical seismicity, and the merging and bending of channels across the fault. The geological activity index of fault F6, which is clear in the seismic profile (Fig. 4) but blurry in the field, is as small as 1, indicative of weak activity and supported by the highly diffused or eroded scarps and the absence of fault traces and historical

seismicity.

Noticeably, although the structural section across the Hero Range shows that fault F6 is the dominant structure and the faults F3 and F4 are back-thrusts (Fig. 4), our observations indicate that faults F3 and F4 are much more active than fault F6 (Table 1). This can be explained by the wedge model in which the lower part of fault F6 and its back-thrusts (F3 and F4) formed a wedge penetrating northeastward beneath and therefore raising the Hero Range (Fig. 4).

4. Geomorphic features

The drainage pattern and three geomorphic indexes, i.e., Hypsometric curves and integral (*HI*), longitudinal and ridge-line channel profiles, and normalized stream length-gradient (*SLK*) index were analyzed for the Hero Range. There are two freely available DEM datasets in the study area: the 90 m SRTM (Shuttle Radar Topography Mission) data and the 30 m ASTER (Advanced Spaceborne Thermal Emission and Reflection Radiometer) data. We chose the SRTM for analysis because it follows the channels more accurately despite its spatial-resolution disadvantages, which is testified by both our experience and previous study (Fisher et al., 2013).

4.1. Drainage pattern

The drainage network was extracted using the Arc Hydro tools on ArcGIS, and 27 major channels as well as their corresponding tributaries and catchments were identified (Fig. 7). We divided the Hero Range into three sectors (west, south, and east) according to the characteristics of the drainage systems. The west sector drains

the entire Shizigou anticline and part of the western flank of the Ganchaigou anticline, and contains channels flowing mainly towards the west or southwest (# 1 – 8) into Gasikule Lake (Figs. 2, 7). The south sector drains the Youshashan anticline and contains generally southward flowing channels (# 9 – 18), again into Gasikule Lake (Figs. 2, 7). Channels in this sector are systematically deflected and form U- and L-shaped turns convex toward the ESE, indicating an ESE-ward growth of the Youshashan anticline (Yin et al., 2007). The east sector drains the Xianshuiquan anticline, the southwestern flank of the Youquanzi anticline and most of the Ganchaigou anticline, and contains channels flowing mainly to the east – northeast (# 19 – 27, Fig. 7). Main drainage divides bounding these three sectors are curved with angles of ca. 90° (Fig. 7), which may be the result of interaction between active faulting and headward erosion.

4.2. Hypsometric curves

The hypsometric curve of a catchment reflects the relative proportion of the watershed area above a given height and is a useful tool for characterizing the topographic relief within a drainage basin (Strahler, 1952). As the watershed area and the height are both normalized to 0 – 1, it can clearly establish comparisons between basins of different sizes (Walcott and Summerfield, 2008; Pérez-Peña et al., 2010; Gao et al., 2013). The shape of a hypsometric curve is related with the stage of topographic development of the basin. Convex curves indicate a relatively youthful (or newly formed) stage; S-shaped curves feature a maturity stage; and concave curves are indicative of a peneplain stage (Strahler, 1952). The hypsometric integral

(*HI*) is defined as the area below the hypsometric curve and varies from 0 to 1 with values close to 1 corresponding to convex curves while those close to 0 indicative of concave curves.

Hypsometric curves and *HI* values were calculated for all the 27 catchments in the Hero Range using the ArcGIS extension developed by Pérez-Peña et al. (2009a). Hypsometric curves show a similar convex-upward feature with an average *HI* value of 0.5 (ranging 0.41 – 0.58) for catchments in the west (#1 – 8) and the south (#9 – 18) sectors (Figs. 8a, 8b, 8d), accounting for an moderately active topography. The hypsometric curves for catchments in the east sector present much more complex shapes (Fig. 8c). Catchment #19 has a concave-shaped curve with a low *HI* value of ~0.36, and catchment #23 has an S-shaped curve, indicating a relatively weakly active topography. The remaining catchments all have convex-shaped hypsometric curves, evidencing active topography. Noticeably, hypsometric curves of the catchments #25, #26 and #27, which are relatively far away from fault F6 and the axis of the Youquanzi anticline (Fig. 7), present much more convex shapes with *HI* values > 0.6, suggesting a much younger topography.

4.3. Longitudinal and ridgeline channel profiles

Longitudinal channel profiles represent the balance between rates of erosion and rock uplift (Sinha and Parker, 1996; Kirby et al., 2003). Channels in a dynamic equilibrium state have concave-upward shapes (Sinha and Parker, 1996). Once this equilibrium is disturbed, for example, by tectonic rock uplift, lithological variation, or base-level lowering, convex-upward steps (knickpoints) will appear on the profiles.

Hence, analysis of longitudinal channel profiles is a useful tool to evaluate and locate tectonic activities of a region if other factors can be excluded (Kirby et al., 2003; Troiani and Della Seta, 2008; Zhang et al., 2011). Ridge-line channel profiles are depicted by getting along-strike elevation of channels from a theoretical pre-incision surface obtained by interpolating the altitudes from present-day ridge lines (or lateral divides) of the drainage basins (Menéndez et al., 2008). Although this interpolated surface is only a proxy for the real pre-incision surface, the height differences between longitudinal channel profiles and corresponding ridge-line profiles can account for the bulk erosion of drainage basins (Menéndez et al., 2008; Zhang et al., 2008; Pérez-Peña et al., 2010).

Longitudinal and ridge-line channel profiles were extracted for all the 27 major channels (Fig. 9). Most longitudinal channel profiles (#1-25) have overarching concave-upward shapes with several knickpoints, demonstrating that the channels are not in an equilibrium state. On longitudinal profiles of channels #1-18 and #22-25, knickpoints coincide well with the active faults traces F3, F4 and F5 (Fig. 9). Longitudinal profiles of channels #26 and #27 show unusually convex-upward shapes, indicating either a more tectonically active setting (Hovius, 2000) or being affected by some other factors.

Differences between longitudinal and corresponding ridge-line profiles reveal that the greatest incision (with values up to 250 m) is located in the midstream to downstream of channels in the west sector (channels #3 – 8), and the upstream and midstream of channels in the east sector (channels #21 – 25). Channel incision values

in the south sector are lower than 150 m (Fig. 9), suggesting a younger topography or shorter incision history.

4.4. Normalized stream-length gradient (SLK) index

The stream-length gradient (*SL*) index is a geomorphic index that has been used widely in morpho-tectonic assessment (Chen et al., 2003; Troiani and Della Seta, 2008; Gao et al., 2013) and follows the equation firstly proposed by Hack (1973) as: $SL = (\Delta H/\Delta L) \times L$, where ΔH is the difference in elevation between the ends of a channel reach under evaluation; ΔL is the length of the reach; and L is the channel length measured from the drainage divide along the longest channel in the catchment to the midpoint of the channel reach (Appendix A1). In order to compare *SL* values of channels with different lengths, the normalized stream-length gradient (*SLK*) index was introduced as dividing *SL* values by a parameter *K* (*SL* / *K*). The *K* parameter is defined as the *SL* index for the entire channel (Chen et al., 2003; Pérez-Peña et al., 2009b) and follows the equation: $K = \Delta H_{total}/(\mathrm{Ln}\ L_{total})$, where ΔH_{total} and L_{total} are the height difference and the length of the whole channel, respectively (Appendix A1). *SLK* index is highly sensitive to changes in channel slope (Chen et al., 2003; Troiani and Della Seta, 2008; Pedrera et al., 2009). Anomalously high *SLK* values usually correspond to the existence of knickpoints, resulting in this index being used widely to detect active tectonics on a specific uniform rock type (Monteiro et al., 2010; Gao et al., 2013).

The *SLK* values were calculated for all the 27 channels as well as some major tributaries in the Hero Range with a constant channel reach of 1000 m, yielding 660

points for analysis (Fig. 9). An *SLK* anomaly map was generated by using a krigging statistic method based on a variogram model (Pérez-Peña et al., 2009b, Appendix A1) (Fig. 10). The result shows that high *SLK* values appear mostly at margins of the Hero Range. Five positive *SLK* anomalies (labeled as A to E) were identified on the map, and most of them coincide with locations of known active faults.

Anomalies A and B are associated with the active Shizigou (F3) and the Youshashan (F4) faults, respectively, along the southwestern edge of the range (Fig. 10). Noticeable is that the anomaly B becomes wider towards the east, resulting possibly from the eastward propagation of the Youshashan anticline (Yin et al., 2007). The relatively smaller anomaly C is located on the hanging wall of the SW-dipping Gandong fault (F5) in the eastern flank of the Ganchaigou anticline (Fig. 10). The remaining area in the east sector of the range is characterized by generally high *SLK* values (mostly > 3.7) with two positive anomalies (D and E). Anomaly D is as much as 12 km wide, located in the hangingwall of the fault F6, and covers most area of the southern Xianshuiquan anticline (Fig. 10). Different from the above four anomalies that lie nearly parallel to the faults or fold axes, anomaly E, which is located in the SE part of the east sector, is oblique to the fault F6 and the axis of the Youquanzi anticline but parallel to the wind direction (Fig. 10).

5. Discussions

5.1. Consistency between the geomorphic and the geological results

Table 1 summaries the result of active tectonics determined from geomorphic

indexes in the Hero Range. Thus a geomorphic activity index was obtained and compared with the corresponding geological activity index to assess their consistency. For simplicity, the east sector was subdivided into three parts (Table1): 1) a western part (W. part) that contains the upstream of channels #21 – 25 draining mainly the Ganchaigou anticline; 2) a northeastern part (NE part) that contains channels #19 and #20 as well as downstream of channels #21 – 24 draining the Xianshuiquan anticline; and 3) a southeastern part (SE part) that contains channels #26 – 27 and downstream of channel #25 draining the southwestern flank of the Youquanzi anticline (Figs. 7, 10).

In the west and south sectors, the geomorphic activity indexes are both 2.67 (Table 1) based on the generally convex-upward hypsometric curves (Figs. 8a, 8b), overall concave-upward longitudinal channel profiles with knickpoints near the channel outlets (Fig. 9), and high *SLK* values in the hangingwall of and very close to the faults (Fig. 10). This attests to strong activity on the Shizigou (F3) and the Youshashan (F4) faults which is consistent with the geological result (Table 1). In the western part of the east sector, the geomorphic activity index is 2 according to the presence of knickpoints on the longitudinal channel profiles (Fig. 9) and the relatively smaller positive *SLK* anomaly C (Fig. 10), indicating that the Gandong fault (F5) is moderately active, which coincides well with the geological result (Table 1).

In the NE part of the east sector, the mostly concave-upward or S-shape hypsometric curves (Fig. 8c), the abundant knickpoints on the longitudinal profiles (Fig. 9) and the unusually wide positive *SLK* anomaly D (Fig.10) generate a

geomorphic activity index of 2.33, indicating moderate activity on the fault F6, which is inconsistent with the geological evidence that indicates weak activity (Table 1). A similar situation occurred in the SE part of the east sector, where highly convex hypsometric curves with large *HI* values (catchments #25 – 27, Figs. 8c, 8d), apparently convex-upward longitudinal channel profiles (channels #26 – 27, Fig. 9) and the positive *SLK* anomaly G (Fig. 10) generated a high geomorphic activity index value of 3, suggesting strongly active tectonics. Again, this conflicts with the geological observations on fault F6 (Table 1).

The above analysis reveals that the active tectonics obtained from geomorphic analysis are consistent with the geological evidence in the west and south sectors as well as the western part of the east sector where fluvial incision is predominant. However, a contradiction occurred between the geomorphic and the geological results, with the former showing much stronger activity, in the NE and the SE parts of the east sector where wind erosion also plays an important role in shaping the landscape. This contradiction is aggravated by the fact that the fault F6, which is the structural boundary along the northeastern side of the Hero Range, is now 3 – 8 km northeast of the northeastern mountain front of the Hero Range (Figs. 5d, 5e, 5h, 7). This suggests that the activity on fault F6 may have a lesser influence on the topography than the Shizigou (F3), the Youshashan (F4) and the Gandong (F5) faults. Therefore, the geomorphic indexes in the NE and the SE parts of the east sector are influenced by factors other than the activity of fault F6, which we interpret as being due to wind erosion. This interpretation is corroborated by two observations. First,

the northeastern margin of the Hero Range is now greatly eroded by winds (Figs. 2, 5d – 5i). Secondly, the positive *SLK* anomaly D did not coincide well with the axis of the Xianshuiquan anticline and anomaly E lies oblique to the fault F6 and axis of the Youquanzi anticline but parallel to the wind direction (Fig. 10), excluding the possibility of sub-surface folding.

5.2. Influence of wind erosion on geomorphic indexes

Through the above analysis, we evaluated the consistency between the geomorphic and the geological evidence, and pointed out that wind erosion could result in misinterpretation of active tectonics as determined from geomorphic indexes. As a result, we proposed a theoretical model to illustrate that the wind erosion may influence the result of geomorphic indexes in the east sector of the Hero Range in two ways.

First, wind erosion lowered the base-level to the northeast of the Hero Range (Fig. 11), as illustrated by the present base-level being >10 m meters lower than that when the remnant alluvial fan was deposited (Fig. 5k). Noticeably, the base-level here doesn't mean the lake-level to which the rivers grade, but a local base-level in the piedmont region on which the rivers flow away from the Hero Range (Fig. S2 in the Appendix A2). The lowering of this local base-level broke the local equilibrium state of the channels, and hence produced knickpoints on the longitudinal channel profiles. These knickpoints firstly occurred near the outlet of the channels, and would retreat upwards because fluvial incision is still an important erosional process in the northeastern side, irrespective of the severe wind erosion along the margin

(Fig. 2). As wind erosion persisted, knickpoints were continuously produced and retreated upstream, forming steeper channel profiles and therefore high *SLK* values in most area of the east sector (Fig. 10). This process also led to the increase of channel incision in the upstream of the channels, which is proven by the topographic relief map (Fig. 12) showing that the largest relief is now located in the vast area of the northeastern side (east sector) with maximum value of ~270 m.

Second, winds removed materials from the Hero Range laterally (Fig. 5k), steepening the mountain front (Fig. 11) and consequently making the hypsometric curves (e.g., the catchments #25 – 27, Fig. 8c) and even the longitudinal channel profiles (e.g., channels #26 – 27, Fig. 9) more convex. Different from the west and south sectors where the present topographic borders follow the structural borders, as much as 8 km distance was measured between the two types of borders in the east sector (Figs. 3f, 5d, 5e, 5h, 12), which we attributed to lateral erosion by winds because the region between is dominated by yardangs (Fig. 11). The lateral erosion is particularly intense in the SE part of the east sector (the core of the Youquanzi anticline was totally flattened), resulting possibly from the original mountain front that should follow the trace of fault F6 being oblique to the wind direction there (Figs. 2, 10, 12). The process of the lateral wind erosion also results in the occurrence of slope breaks separating a southeastward-narrowing flat region to the southwest and a steep region to the northeast (Fig. 11), which are so clearly evident on the swath elevation profiles across the east sector of the Hero Range (Figs. 3d – 3f).

6. Conclusion

Geological and geomorphologic features were studied in detail to reveal active tectonics in the Hero Range, and to evaluate whether geomorphic indexes are feasible for detecting active tectonics in extremely arid area where wind erosion plays an important role. The following conclusions are drawn:

(1) In the west and south sectors, as well as the western part of the east sector of the Hero Range, where fluvial incision prevails, hypsometric curves are convex, knickpoints are common on longitudinal channel profiles and positive anomalies of the normalized stream gradient-length (*SLK*) values are present in the hanging walls of and close to the faults. All are indicative of active faulting on the Shizigou (F3), the Youshashan (F4) and the Gandong faults (F5), consistent with the geological evidence from fault traces and scarps, faulted Holocene fans and historical seismicity within the past four decades.

(2) Along the NE and the SE parts of the east sector where wind erosion is as prominent as fluvial incision, contradiction was observed between the geomorphic data favoring moderately to strongly active tectonics, and the geological evidence showing weak activity on the boundary fault (F6).

(3) The contradiction results probably from the wind erosion caused by northwesterly winds in two ways. First, it lowered the base-level to the northeast, producing knickpoints on the longitudinal channel profiles and thus positive *SLK* anomalies parallel to the wind direction rather than the fault extension. Second, it eroded the Hero Range laterally, steepening the mountain front and consequently

making the hypsometric curves and even the longitudinal profiles more convex. That is to say, wind erosion tends to make geomorphic indexes exhibit anomalous values that are indicative of greater tectonic activity, resulting in their ineffectiveness as indicators of active tectonics in extremely arid regions with severe wind erosion.

Acknowledgement: This paper benefited a lot from suggestions of Dr. Eric Cowgill and Michael Oskin in University of California at Davis and Dr. Huiping Zhang in China Earthquake Administration, and is supported by the National Natural Science Foundation of China (Grant No. 41372206 and No. 41330207) and the Fundamental Research Funds for the Central Universities (Grant No. 2014QNA3011). The authors appreciate Dr. Andrew James Plater, Dr. José Vicente Pérez-Peña and another anonymous reviewer for their helpful comments.

References

Avouac, J. and Peltzer, G., 1993. Active tectonics in southern Xinjiang, China: Analysis of terrace riser and normal fault scarp degradation along the Hotan-Qira Fault System. Journal of Geophysical Research: Solid Earth (1978-2012) 98(B12): 21773-21807.

Azanon, J.M., Perez-Pena, J.V., Giaconia, F., Booth-Rea, G., Martinez-Martinez, J.M. and Rodriguez-Peces, M.J., 2012. Active tectonics in the central and eastern Betic Cordillera through morphotectonic analysis: the case of Sierra Nevada and Sierra Alhamilla. Journal of Iberian Geology 38(1SI): 225-238.

Bishop, P., 2007. Long-term landscape evolution: linking tectonics and surface processes. Earth Surface Processes and Landforms 32(3): 329-365. Doi:10.1002/esp.1493.

Burbank, D.W. and Anderson, R.S., 2012. Tectonic Geomorphology. Wiley-Blackwell, 1-16 pp.

Chen, Y.C., Sung, Q.C. and Cheng, K.Y., 2003. Along-strike variations of morphotectonic features in the Western Foothills of Taiwan: tectonic implications based on stream-gradient and hypsometric analysis. Geomorphology 56(1-2): 109-137.

Chen, Z., Xiao, A., Zhou, S. and He, G., 2005. The main control factor for Jurassic distribution in Qaidam basin. Earth Science Frontiers 12(3): 149-155 (in Chinese with English abstract).

Clark, M.K., Schoenbohm, L.M., Royden, L.H., Whipple, K.X., Burchfiel, B.C., Zhang, X., Tang, W., Wang, E. and Chen, L., 2004. Surface uplift, tectonics, and erosion of eastern Tibet from large-scale drainage patterns. Tectonics 23(1): TC1006. Doi:10.1029/2002TC001402.

DiBiase, R.A., Whipple, K.X., Heimsath, A.M. and Ouimet, W.B., 2010. Landscape form and millennial

erosion rates in the San Gabriel Mountains, CA. Earth and Planetary Science Letters 289(1): 134-144.

England, P. and Molnar, P., 1990. Surface uplift, uplift of rock, and exhumation of rocks. Geology 18(12): 1173-1177. Doi:10.1130/0091-7613(1990)018<1173:SUUORA>2.3.CO;2.

Fisher, G.B., Bookhagen, B. and Amos, C.B., 2013. Channel planform geometry and slopes from freely available high-spatial resolution imagery and DEM fusion: Implications for channel width scalings, erosion proxies, and fluvial signatures in tectonically active landscapes. Geomorphology 194: 46-56.

Gao, M., Zeilinger, G., Xu, X., Wang, Q. and Hao, M., 2013. DEM and GIS analysis of geomorphic indices for evaluating recent uplift of the northeastern margin of the Tibetan Plateau, China. Geomorphology 190: 61-72.

Garcia, M. and Herail, G., 2005. Fault-related folding, drainage network evolution and valley incision during the Neogene in the Andean Precordillera of Northern Chile. Geomorphology 65(3-4): 279-300.

Goudie, A. S., 2008, The History and Nature of Wind Erosion in Deserts. Annual Review of Earth and Planetary Sciences 36: 97-119. Doi: 10.1146/annurev.earth.36.031207.124353.

Hack, J.T., 1973. Stream-profile analysis and stream-gradient index. J. Res. US Geol. Surv 1(4): 421-429.

Heermance, R.V., Pullen, A., Kapp, P., Garzione, C.N., Bogue, S., Ding, L. and Song, P., 2013. Climatic and tectonic controls on sedimentation and erosion during the Pliocene – Quarternary in the Qaidam Basin (China). Geological Society of America Bulletin 125(5-6): 833-856. Doi:10.1130/B30748.1.

Hilley, G.E. and Arrowsmith, J.R., 2008. Geomorphic response to uplift along the Dragon's Back pressure ridge, Carrizo Plain, California. Geology 36(5): 367-370.

Hovius, N., 2000. Macroscale Process Systems of Mountain Belt Erosion. In M.A. Summerfield (Ed.), Geomorphology and Global Tectonics. John Wiley & Sons Ltd, Chichester, pp. 77-105

Jackson, J., Norris, R. and Youngson, J., 1996. The structural evolution of active fault and fold systems in central Otago, New Zealand: evidence revealed by drainage patterns. Journal of Structural Geology 18(2 – 3): 217-234.

Kapp, P., Pelletier, J.D., Rohrmann, A., Heermance, R., Russell, J. and Ding, L., 2011. Wind erosion in the Qaidam basin, central Asia: Implications for tectonics, paleoclimate, and the source of the Loess Plateau. GSA Today 21(4-5): 4-10.

Keller, E.A., Seaver, D.B., Laduzinsky, D.L., Johnson, D.L. and Ku, T.L., 2000. Tectonic geomorphology of active folding over buried reverse faults: San Emigdio Mountain front, southern San Joaquin Valley, California. GSA Bulletin 112(1): 86-97.

Kirby, E., Whipple, K.X., Tang, W. and Chen, Z., 2003. Distribution of active rock uplift along the eastern margin of the Tibetan Plateau: Inferences from bedrock channel longitudinal profiles. Journal of Geophysical Research 108(B4): 2217. Doi:10.1029/2001JB000861.

Liu, Z., Wang, F., Liu, Y., Zhao, C., Gao, J. and Wan, C., 2009. Structural Features and Determination of Deformation Time in the Nanyishan-Jiandingshan Area of Qaidam Basin. Journal of Jilin University (Earth Science Edition) 39(5): 796-802 (in Chinese with English abstract).

Malik, J.N. and Mohanty, C., 2007. Active tectonic influence on the evolution of drainage and landscape: Geomorphic signatures from frontal and hinterland areas along the Northwestern Himalaya, India. Journal Of Asian Earth Sciences 29(5-6): 604-618.

Melosh, B.L. and Keller, E.A., 2013. Effects of active folding and reverse faulting on stream channel

evolution, Santa Barbara Fold Belt, California. Geomorphology 186: 119-135.

Menéndez, I., Silva, P.G., Martín-Betancor, M., Pérez-Torrado, F.J., Guillou, H. and Scaillet, S., 2008. Fluvial dissection, isostatic uplift, and geomorphological evolution of volcanic islands (Gran Canaria, Canary Islands, Spain). Geomorphology 102(1): 189-203. Doi:10.1016/j.geomorph.2007.06.022.

Monteiro, K.D.A., Missura, R. and Correa, A.C.D.B., 2010. Application of the Hack Index - or Stream Length-Gradient Index (SL Index) - to the Tracunhaem River Watershed, Pernambuco, Brazil. Geociências 29(4): 533-539.

Pedrera, A., Pérez-Peña, J.V., Galindo-Zaldívar, J., Azañón, J.M. and Azor, A., 2009. Testing the sensitivity of geomorphic indices in areas of low-rate active folding (eastern Betic Cordillera, Spain). Geomorphology 105(3-4): 218-231.

Pérez-Peña, J.V., Azañón, J.M. and Azor, A., 2009a. CalHypso: An ArcGIS extension to calculate hypsometric curves and their statistical moments. Applications to drainage basin analysis in SE Spain. Computers & Geosciences 35(6): 1214-1223.

Pérez-Peña, J.V., Azañón, J.M., Azor, A., Delgado, J. and González-Lodeiro, F., 2009b. Spatial analysis of stream power using GIS: SLk anomaly maps. Earth Surface Processes and Landforms 34(1): 16-25.

Pérez-Peña, J.V., Azor, A., Azañón, J.M. and Keller, E.A., 2010. Active tectonics in the Sierra Nevada (Betic Cordillera, SE Spain): Insights from geomorphic indexes and drainage pattern analysis. Geomorphology 119(1-2): 74-87.

Pullen, A., Kapp, P., McCallister, A.T., Chang, H., Gehrels, G.E., Garzione, C.N., Heermance, R.V. and Ding, L., 2011. Qaidam Basin and northern Tibetan Plateau as dust sources for the Chinese Loess Plateau and paleoclimatic implications. Geology 39(11): 1031-1034.

Rieser, A.B., Neubauer, F., Liu, Y. and Ge, X., 2005. Sandstone provenance of north-western sectors of the intracontinental Cenozoic Qaidam basin, western China: Tectonic vs. climatic control. Sedimentary Geology 177(1-2): 1-18. Doi:10.1016/j.sedgeo.2005.01.012.

Rohrmann, A., Heermance, R., Kapp, P. and Cai, F., 2013. Wind as the primary driver of erosion in the Qaidam Basin, China. Earth and Planetary Science Letters 374: 1-10. Doi:10.1016/j.epsl.2013.03.011.

Seeber, L. and Gornitz, V., 1983. River profiles along the Himalayan Arc as indicators of active tectonics. Tectonophysics 92(4): 335-367.

Sinha, S.K. and Parker, G., 1996. Causes of concavity in longitudinal profiles of rivers. Water Resources Research 32(5): 1417-1428.

Strahler, A.N., 1952. Hypsometric (area-altitude) analysis of erosional topography. GSA Bulletin 63(11): 1117-1142.

Taylor, M. and Yin, A., 2009. Active structures of the Himalayan-Tibetan orogen and their relationships to earthquake distribution, contemporary strain field, and Cenozoic volcanism. Geosphere 5(3): 199-214.

Troiani, F. and Della Seta, M., 2008. The use of the Stream Length – Gradient index in morphotectonic analysis of small catchments: A case study from Central Italy. Geomorphology 102(1): 159-168.

Walcott, R.C. and Summerfield, M.A., 2008. Scale dependence of hypsometric integrals: An analysis of southeast African basins. Geomorphology 96(1 – 2): 174-186. Doi:10.1016/j.geomorph.2007.08.001.

Wu, L., Xiao, A., Wang, L., Shen, Z., Zhou, S., Chen, Y., Wang, L., Liu, D. and Guan, J., 2011. Late

Jurassic – Early Cretaceous Northern Qaidam Basin, NW China: implications for the Earliest Cretaceous intracontinental tectonism. Cretaceous Research 32(4): 552-564. Doi:10.1016/j.cretres.2011.04.002.

Wu, L., Xiao, A., Yang, S., Wang, L., Mao, L., Wang, L., Dong, Y. and Xu, B., 2012b. Two-stage evolution of the Altyn Tagh Fault during the Cenozoic: new insight from provenance analysis of a geological section in NW Qaidam Basin, NW China. Terra Nova 24(5): 387-395. Doi:10.1111/j.1365-3121.2012.01077.x.

Wu, L., Xiao, A.C., Wang, L.Q., Mao, L.G., Wang, L., Dong, Y.P. and Xu, B., 2012a. EW-trending uplifts along the southern side of the central segment of the Altyn Tagh Fault, NW China: insight into the rising mechanism of the Altyn Mountain during the Cenozoic. Science China Earth Science 55(6): 926-939. Doi:10.1007/s11430-012-4402-7.

Wu, L., Gong, Q. and Qin, S., 2013. When did Cenozoic left-slip along the Altyn Tagh Fault initiate? A comprehensive approach. Acta Petrologica Sinica 29(8): 2837-2850 (in Chinese with English abstract).

Wu, L., Xiao, A., Ma, D., Li, H., Xu, B., Shen, Y. and Mao, L., 2014. Cenozoic fault systems in southwest Qaidam Basin, northeastern Tibetan Plateau: geometry, temporal development and significance for hydrocarbon accumulation. AAPG Bulletin 98(6): 1213-1234. Doi: 10.1306/11131313087

Yin, A., Dang, Y., Zhang, M., Chen, X. and McRivette, M.W., 2008. Cenozoic tectonic evolution of the Qaidam basin and its surrounding regions (Part 3): Structural geology, sedimentation, and regional tectonic reconstruction. GSA Bulletin 120(7-8): 847-876. Doi:10.1130/B26232.1.

Yin, A., Dang, Y., Zhang, M., McRivette, M.W., Burgess, W.P. and Chen, X., 2007. Cenozoic tectonic evolution of Qaidam Basin and its surrounding regions (Part 2): Wedge tectonics in southern Qaidam Basin and the eastern Kunlun Range. Geological Society of America Special Paper 433: 369-390. Doi:10.1130/2007.2433(18).

Zhang, H., Zhang, P., Wu, Q. and Chen, Z., 2008. Characteristics of the Huanghe river longitudinal profiles around Xunhua - Guide area (NE Tibet) and their tectonic significance. Quaternary Sciences 28(2): 299-309 (in Chinese with English abstract).

Zhang, H., Zhang, P. and Fan, Q., 2011. Initiation and recession of the fluvial knickpoints: A case study from the Yalu River-Wangtian’e volcanic region, northeastern China. Science China Earth Sciences 54(11): 1746-1753. Doi:10.1007/s11430-011-4254-6.

Zhang, W., Fang, X., Song, C., Appel, E., Yan, M. and Wang, Y., 2013. Late Neogene magnetostratigraphy in the western Qaidam Basin (NE Tibetan Plateau) and its constraints on active tectonic uplift and progressive evolution of growth strata. Tectonophysics 599: 107-116. Doi:10.1016/j.tecto.2013.04.010.

Figure captions

Fig. 1 (a) Active faults superimposed on the DEM map of the Tibetan Plateau and adjacent areas (Taylor and Yin, 2009), showing the location of western Qaidam Basin.

DEM map is generated from the 90m SRTM data, the same for Fig. 2. EKQ, East Kunlun – Qiman Tagh Mountain; QB, Qaidam Basin; QL, Qilian Mountain. **(b)** Simplified geological map of the western Qaidam Basin (the location is shown in Fig. 1a).

Fig. 2 Major folds, active faults, historical (1973 – 2013) seismicity and wind direction superimposed on the DEM map of the northwestern half of the Hero Range and adjacent area (the location is shown in Fig. 1b). The white shaded area in the Pingding Shan is higher than 4000 m with peak of 4786m. Data of historical seismicity are from http://earthquake.usgs.gov/earthquakes/eqarchives/epic/ (accessed on July 7th 2013). Active faults: F1, Caishiling fault; F2, Cainan fault; F3, Shizigou fault; F4, Youshashan fault; F5, Gandong fault; F6, Yinbei fault. Anticlines: 1, Shizigou anticline; 2, Youshashan anticline; 3, Ganchaigou anticline; 4, XIanshuiquan anticline; 5, Youquanzi anticline. Zones of different erosion types: I, fluvial incision with slight wind deflation; II, fluvial incision and wind deflation; III, dominant wind erosion.

Fig. 3 Swath elevation profiles with locations of major faults and fold axes in the Hero Range and the adjacent areas (for location, see Figs. 1b, 2). Symbols of faults are same as those in Fig. 2. Note the slope breaks in (d), (e) and (f).

Fig. 4 A seismic profile with geological interpretation showing the subsurface structure across the Hero Range (For location, see Fig. 2). Layers labeled as 1 – 8 are Mesozoic – Cenozoic strata: 1, Jurassic - Cretaceous; 2 – 3, Paleocene – Eocene; 4, Oligocene; 5 – 6, early – middle Miocene; 7, late Miocene – middle Pliocene; 8, late Pliocene – Holocene. Symbols of faults are same as those in Fig. 2.

Fig. 5 Photos and images showing fluvial incision and wind erosion (mainly by deflation) in the Hero Range (locations of Figs. 5a – 5e and 5h are shown in Fig. 2). **(a)** Fluvial incision in the Ganchaigou anticline (white arrows mark the location of the main channels). **(b)** Fluvial incision in the southern side of the Hero Range. **(c)** Fluvial

channels in the Youshashan anticline with channel incision ca. 20m. **(d)** and **(e)** Images from Google Earth showing the highly eroded northeastern edge of the Hero Range by winds, and some remnant alluvial fans. **(f)** Steep cliffs and yardangs define the northeastern edge of the Hero Range, indicating the original edge was greatly eroded by winds. The location is shown in Fig. 5e. **(g)** A photo taken in 2008 showing the eroded northeastern edge, the Yardangs and a remnant alluvial-fan. The location is shown in Fig. 5e, and the photographer stood on the top of the remnant alluvial fan. **(h)** An image from Google Earth showing sand dunes and landforms deflated by winds in the northeastern side. **(i)** A photo taken in 2008 showing sand dunes along the northeastern margin. The location is shown in Fig. 5h. **(j)** An image from Google Earth showing in detail a remnant alluvial fan, the location is shown in Fig. 5e. **(k)** A schematic elevation profile across the remnant fan in Fig. 5j, with simplified interpretation. The shallow grey portion denotes those existing during the formation of the fan but subsequently removed by winds. Note that (1) the present-day topographic NE boundary is now 3-8 km southwest away from the structural NE boundary (F6) in (d), (e) and (h), indicative of the lateral erosion by winds; and (2) the old fans in (k), without any surrounding faults, were deposited on a base-level tens of meters higher than the present base-level, evident for base-level lowering by winds over time.

Fig. 6 Active tectonics in the Hero Range (locations of Figs. 6a – 6d, 6g and 6f are shown in Fig. 2). **(a)** Image from Google Earth (3-times exaggeration vertically) showing the scarps of the Shizigou fault (F3) which have been slightly diffused. View towards northeast. **(b)** Image from Google Earth (3-times exaggeration vertically) showing the obvious scarps of the Youshashan fault (F4), and black arrows point out the fault trace. View towards north-northeast. **(c)** and **(d)** Remote sensing images and geological interpretations of the westernmost part of the Youshashan anticline, respectively, showing faulted Pleistocene – Holocene alluvial fans. Qao, Old alluvial fans; Qay, young alluvial fans; SC, salt crust. **(e)** Elevation profiles across the westernmost part of the Youshashan fault (their locations are shown in Figs. 6c, 6d),

showing that the fault F4 faulted the fans with vertical throws generally decreasing westwards. **(f)** The geological section (2-times exaggeration vertically) across the Ganchaigou anticline and the Gandong fault (F5), showing that the strata in the hanging wall are much steeper (70°) than that in the footwall (~15°). **(g)** An image from Google Earth showing the trace of the Gandong fault (F5). Note that the merging and bending of channels across the fault (marked by black arrows) indicate that fault F5 may be active. **(h)** and **(i)** Images from Google Earth (3-times exaggeration vertically) showing the possible scarps of fault F6 separating the Xianshuiquan and the Youquanzi anticlines from the modern salt playa. Note that the scarp has been highly diffused and eroded. The location is shown in Fig. 5d and Fig. 5h, respectively.

Fig. 7 Shaded relief map with the drainage network, the axes of anticlines and major faults in the Hero Range. Numbers indicate the selected main catchments and the corresponding main channels inside. Symbols of faults and anticlines are same as those in Fig. 2.

Fig. 8 Hypsometric curves for the catchments in the west **(a)**, the south **(b)** and the east **(c)** sectors of the Hero Range and their corresponding hypsometric integrals **(d)**. Results are calculated using SRTM DEM and CalHypso ArcGIS module (Pérez-Peña et al., 2009a).

Fig. 9 Longitudinal and ridgeline channel profiles as well as normalized stream length-gradient (*SLK*) index for channels in the Hero Range, showing a good correlation between knickpoints and high *SLK* values. The *SLK* values are calculated with a constant channel reach of 1000m. Symbols of faults are same as those in Fig. 2.

Fig. 10 *SLK* map of the Hero Range generated by using a krigging method based on a variogram model. Five positive *SLK* anomalies (labeled as A – E) are detected.

Symbols of faults and folds are same as those in Fig. 2.

Fig. 11 The schematic model showing the wind-erosion process along the northeastern margin of the Hero Range. Continuous base-level lowering and lateral erosion of mountain front caused by wind erosion generated knickpoints and steepened the mountain front, resulting in high *SLK* values (Fig. 10) and more convex hypsometric curves (Fig. 8c) in the east sector of the Hero Range. Note that (1) the knickpoints continuously retreated upstream because fluvial incision is also an important erosional process there, increasing the channel incision upstream; and (2) lateral erosion created an obvious slope break separating the steep mountain front to the northeast and relatively flat region to the southwest.

Fig. 12 Topographic relief of the Hero Range calculated by a 500 m × 500 m window on the 90 m SRTM DEM data, superimposed by geological features (faults and folds) as well as the present-day topographic (blue heavy dotted line) and the structural (blue heavy solid line, fault F6) NE borders of the Hero Range. We interpreted that the region between the two edges are flattened by wind erosion. Another noticeable thing is that the vast area of the east sector of the Hero Range is of quite large topographic relief, which we regarded as the result of knickpoints retreating upstream triggered by continuous base-level lowering caused by wind erosion. Symbols of faults are same as those in Fig. 2.

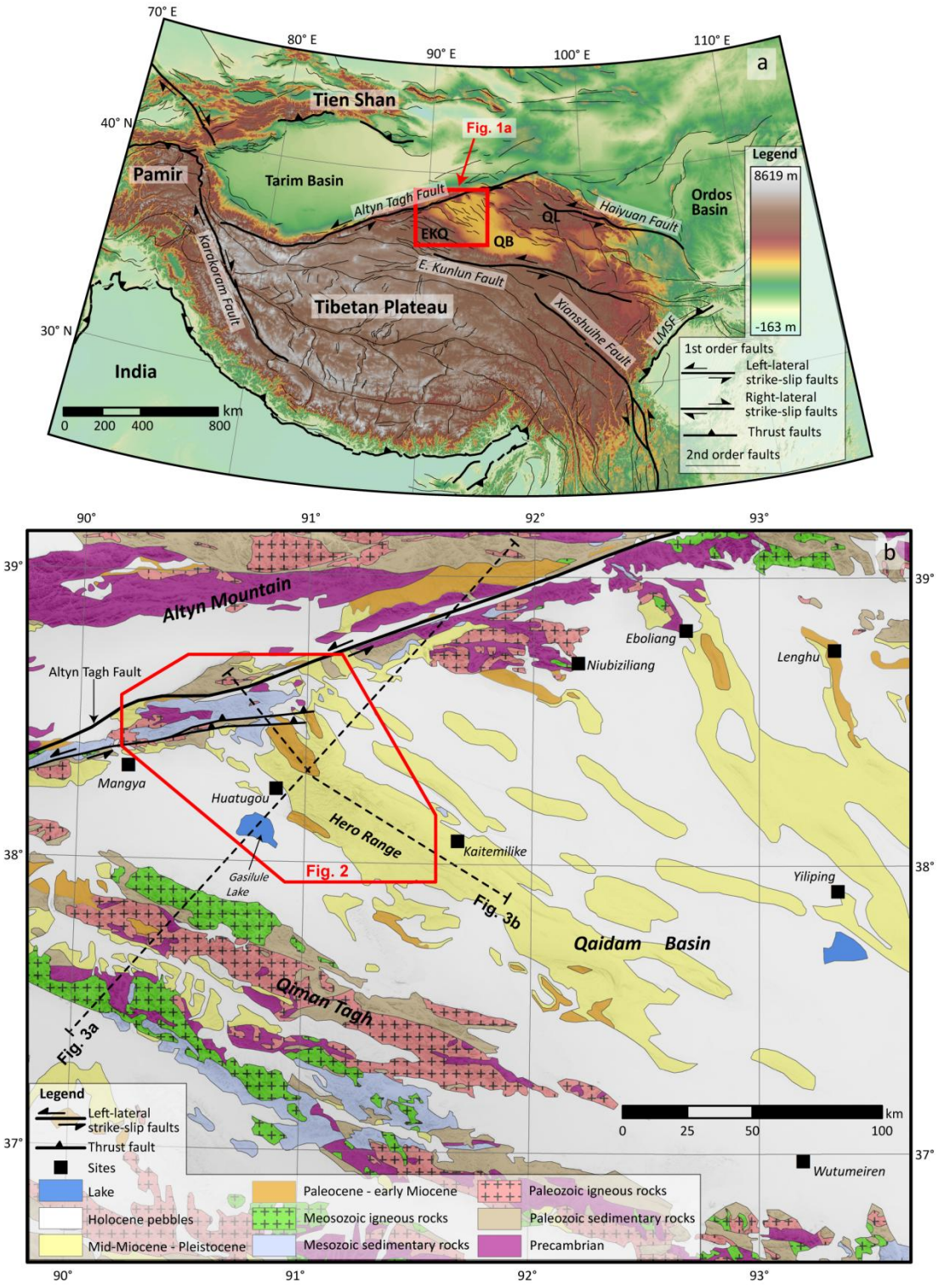

Fig. 1

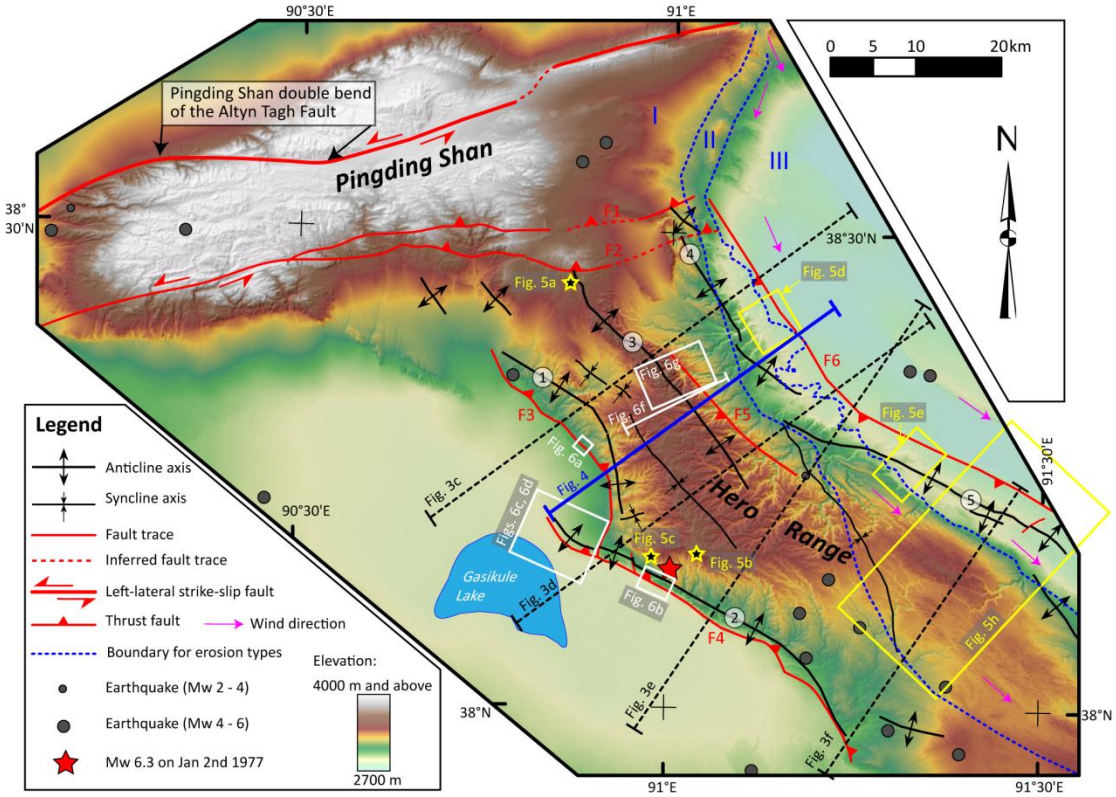

Fig. 2

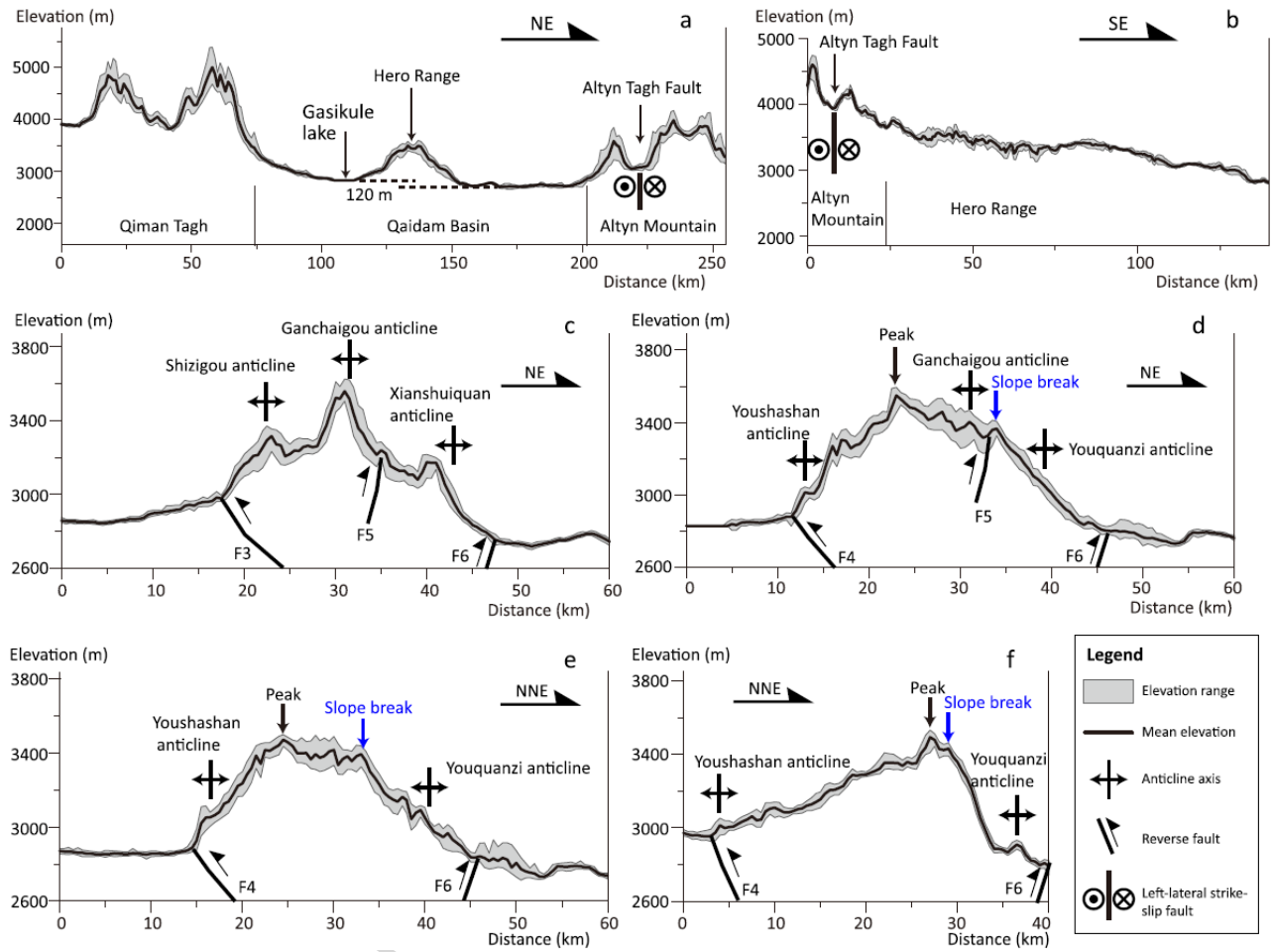

Fig. 3

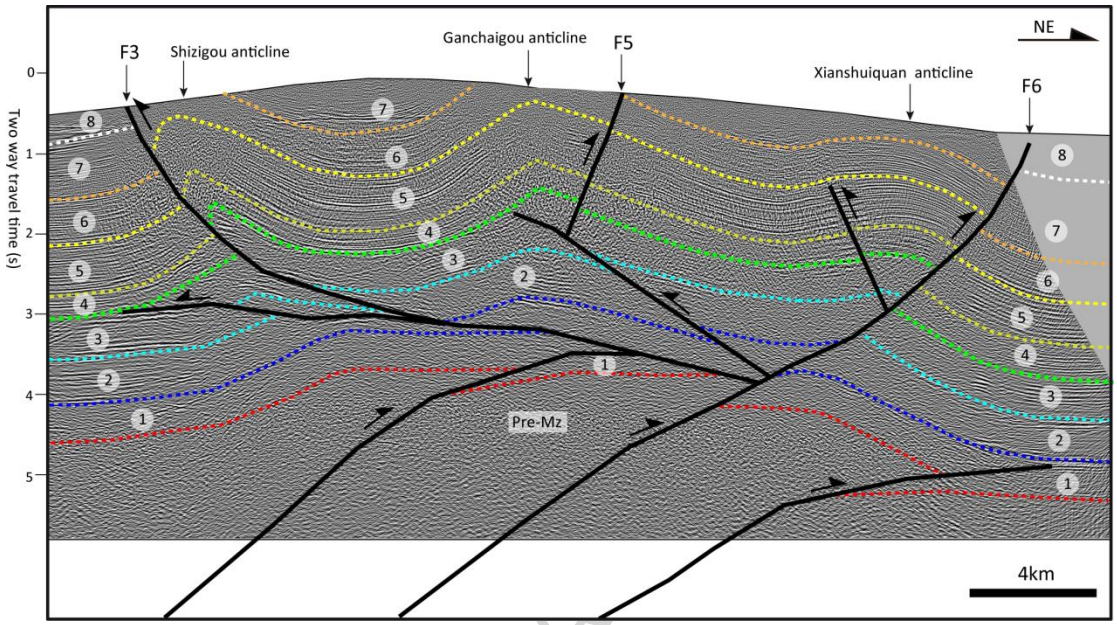

Fig. 4

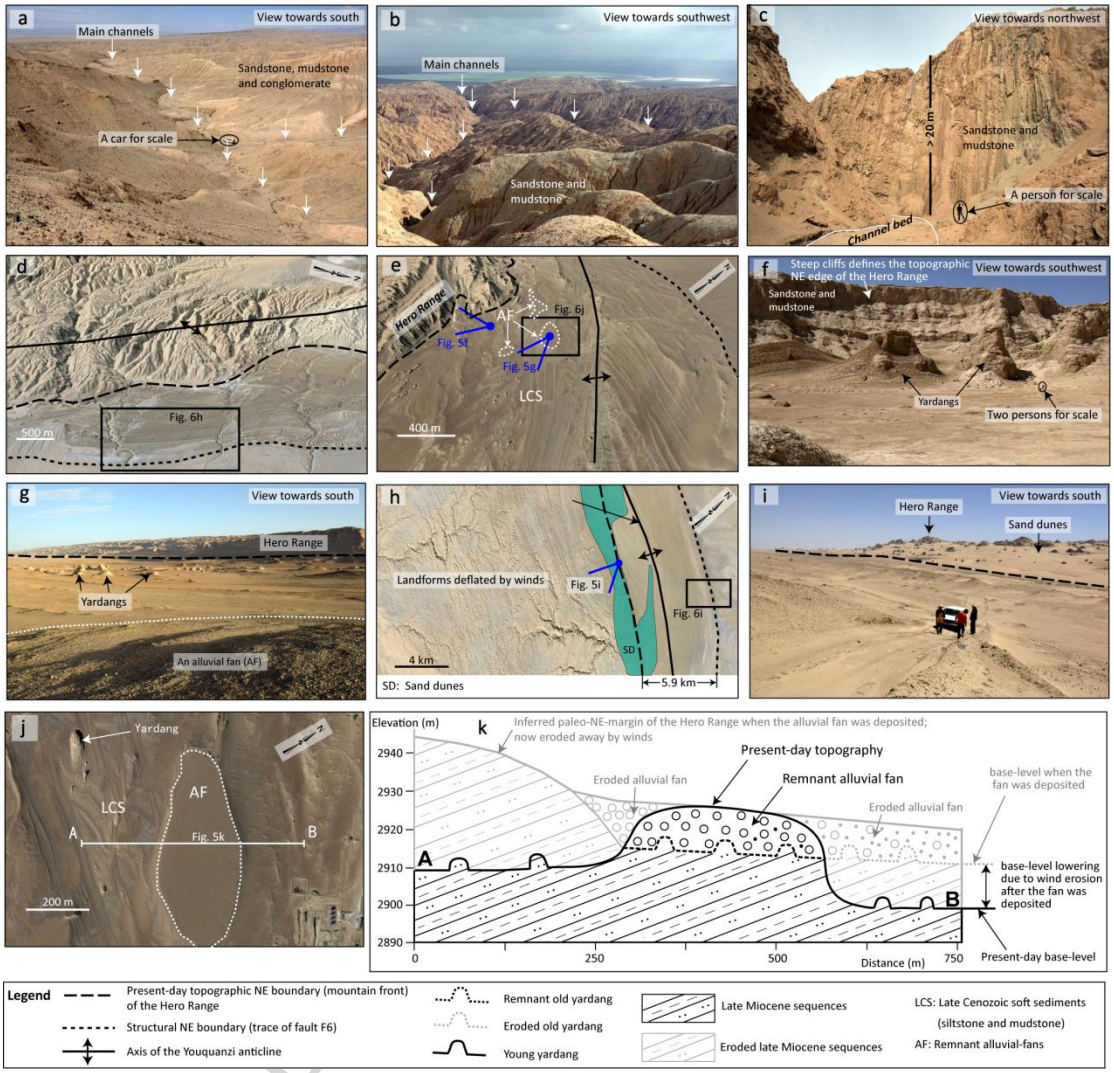

Fig. 5

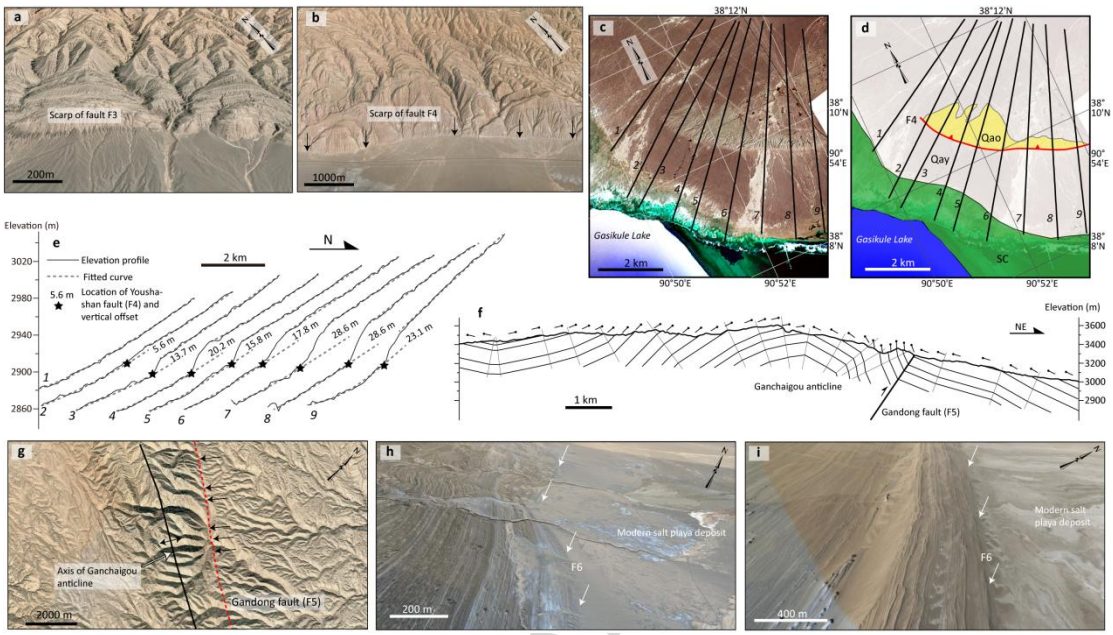

Fig. 6

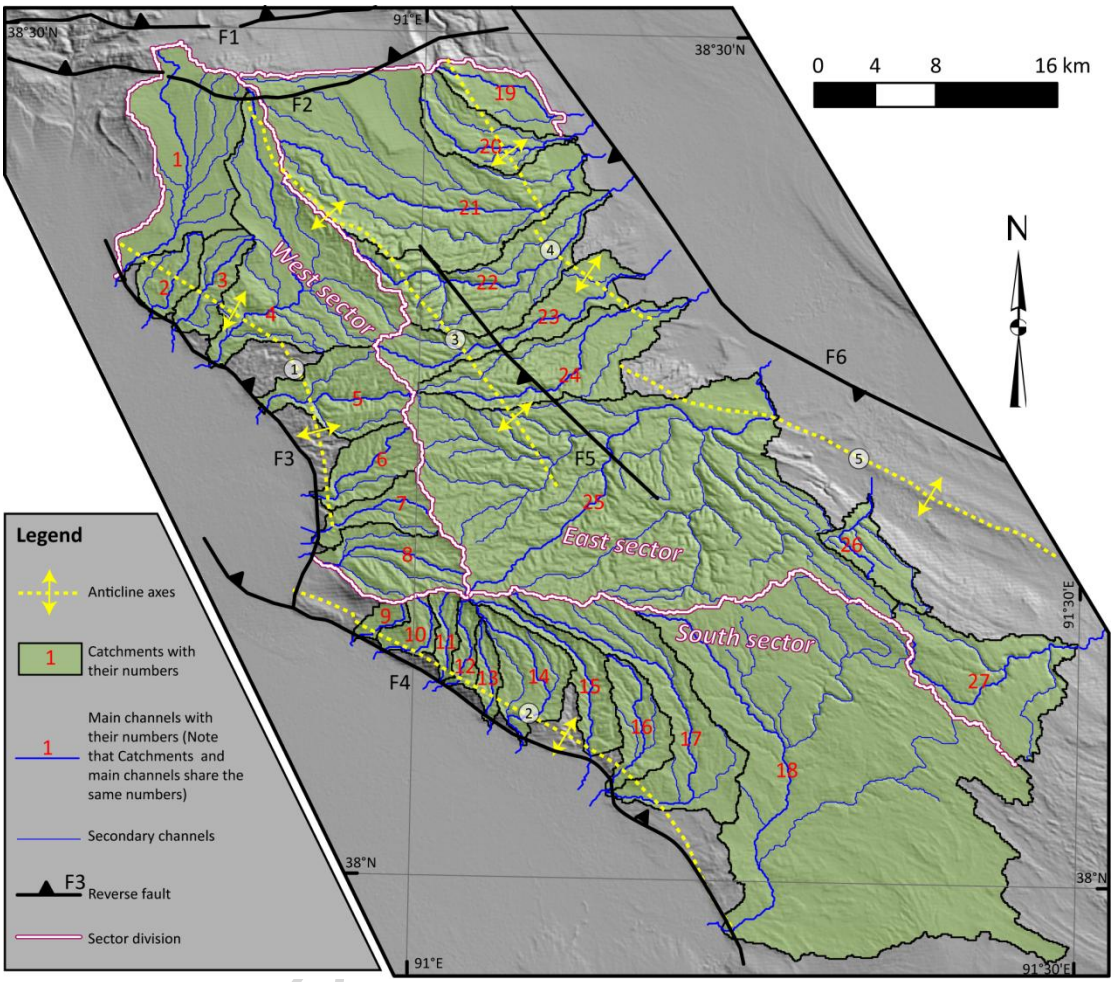

Fig. 7

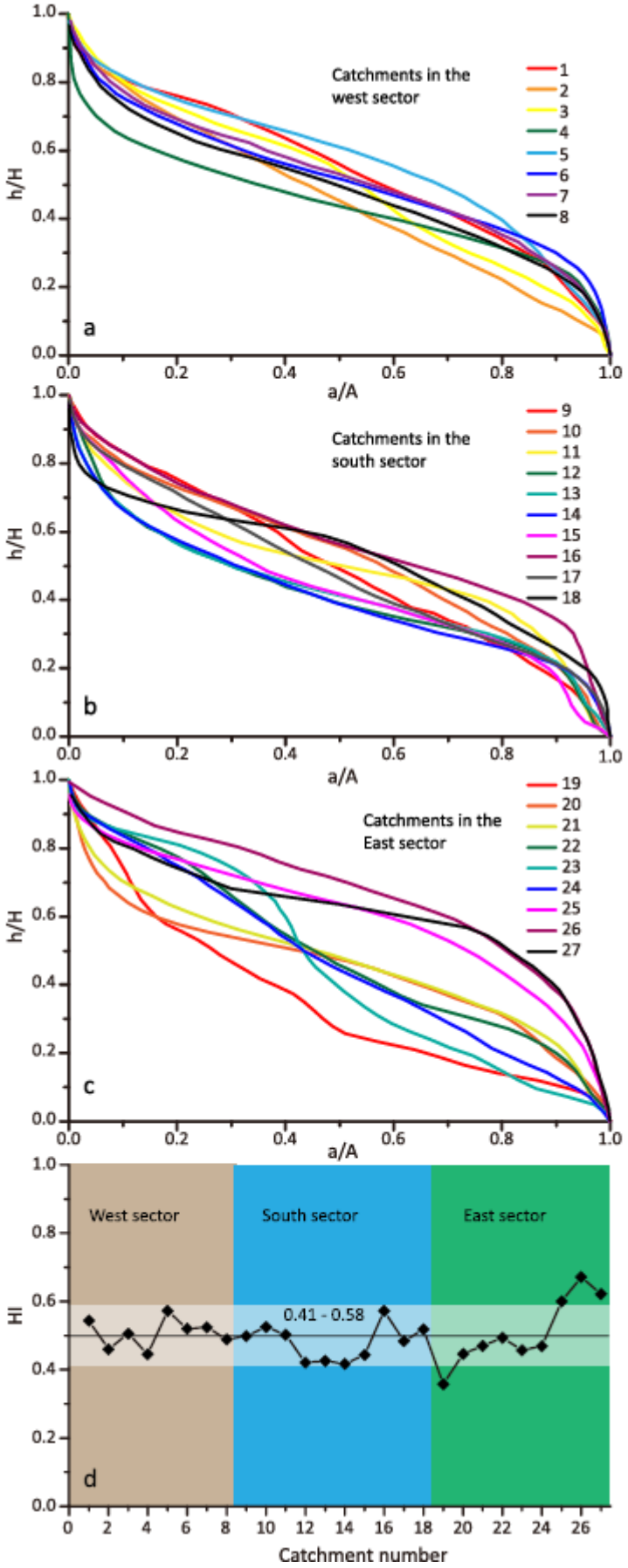

Fig. 8

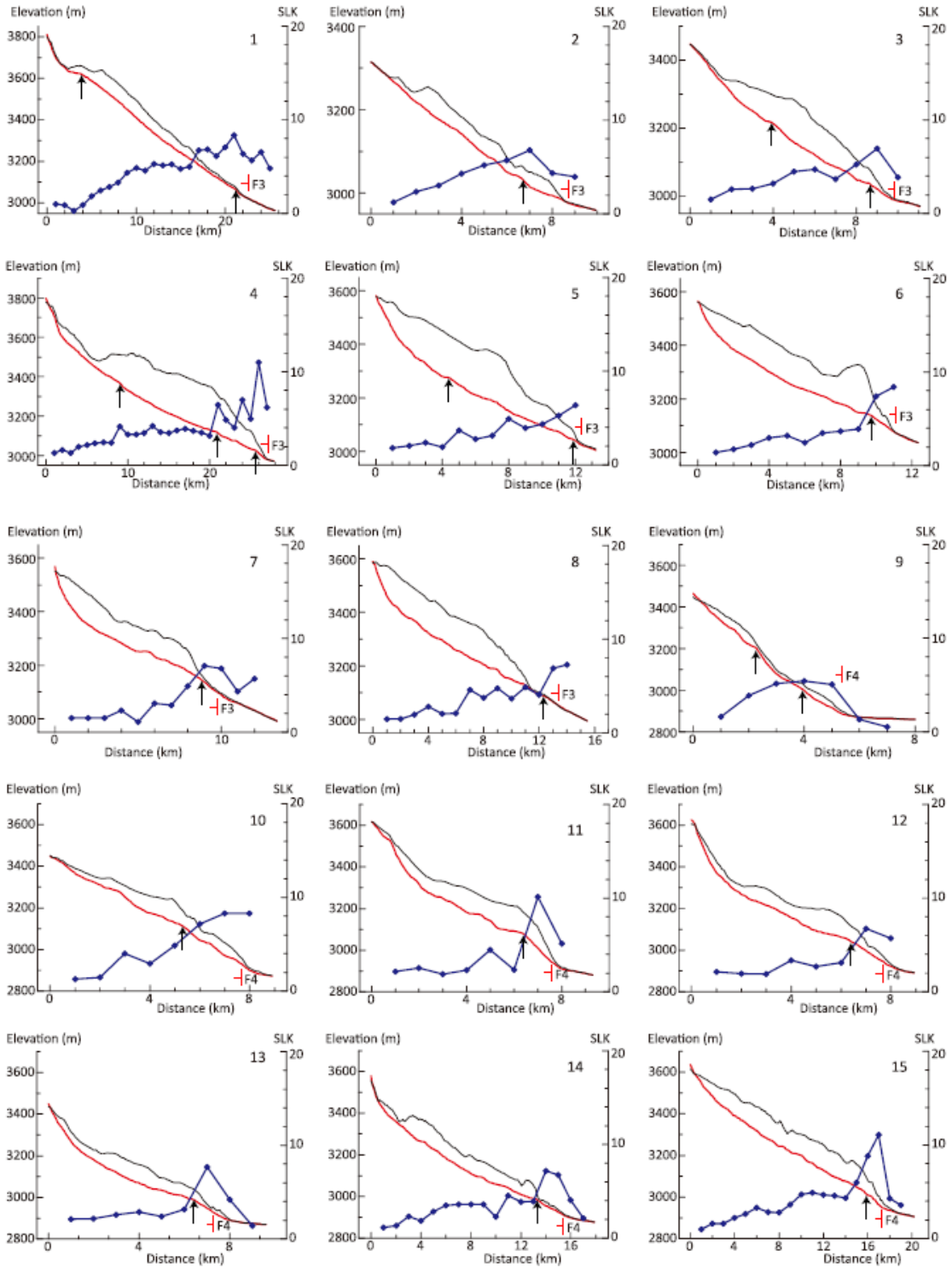

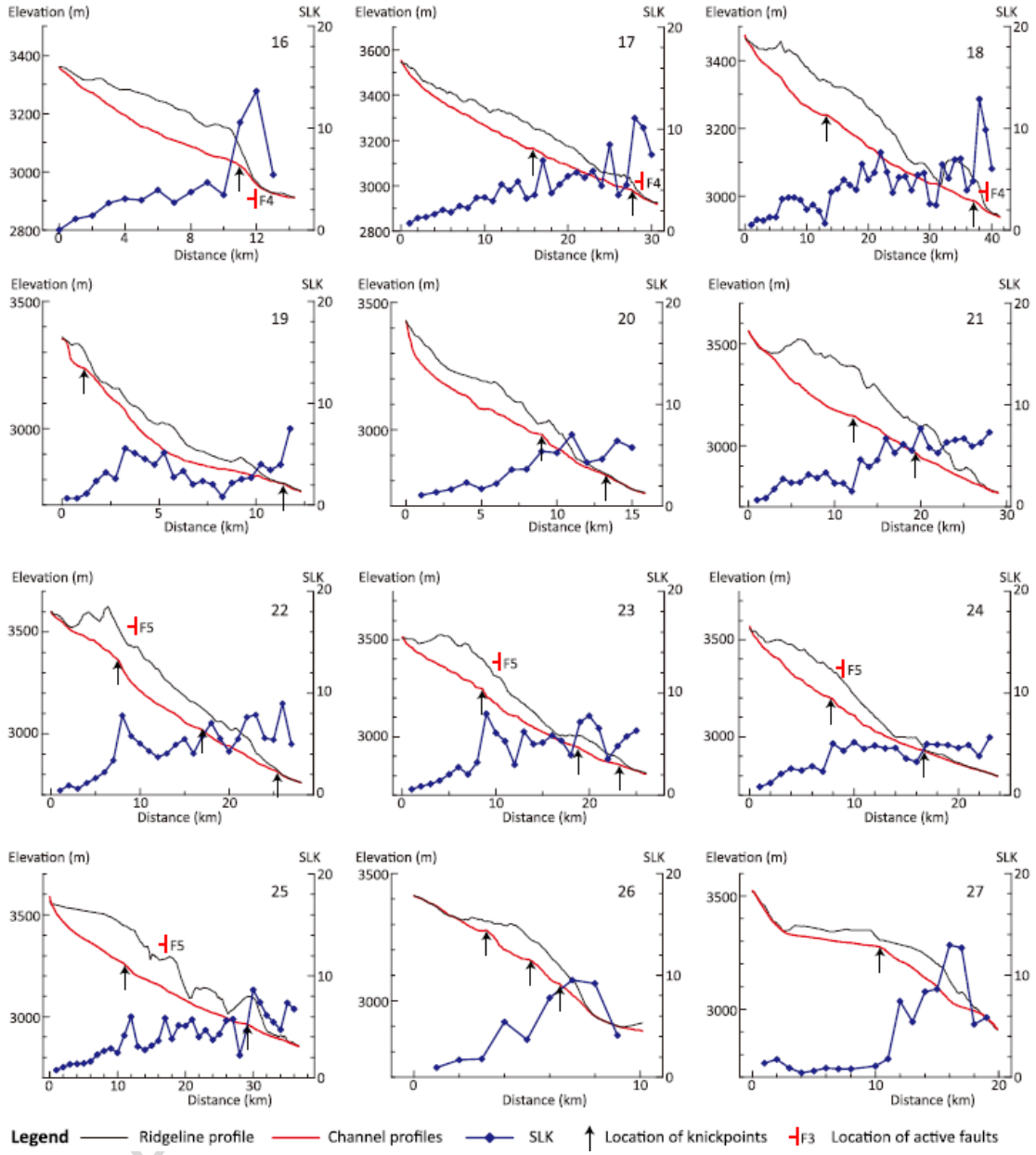

Fig. 9

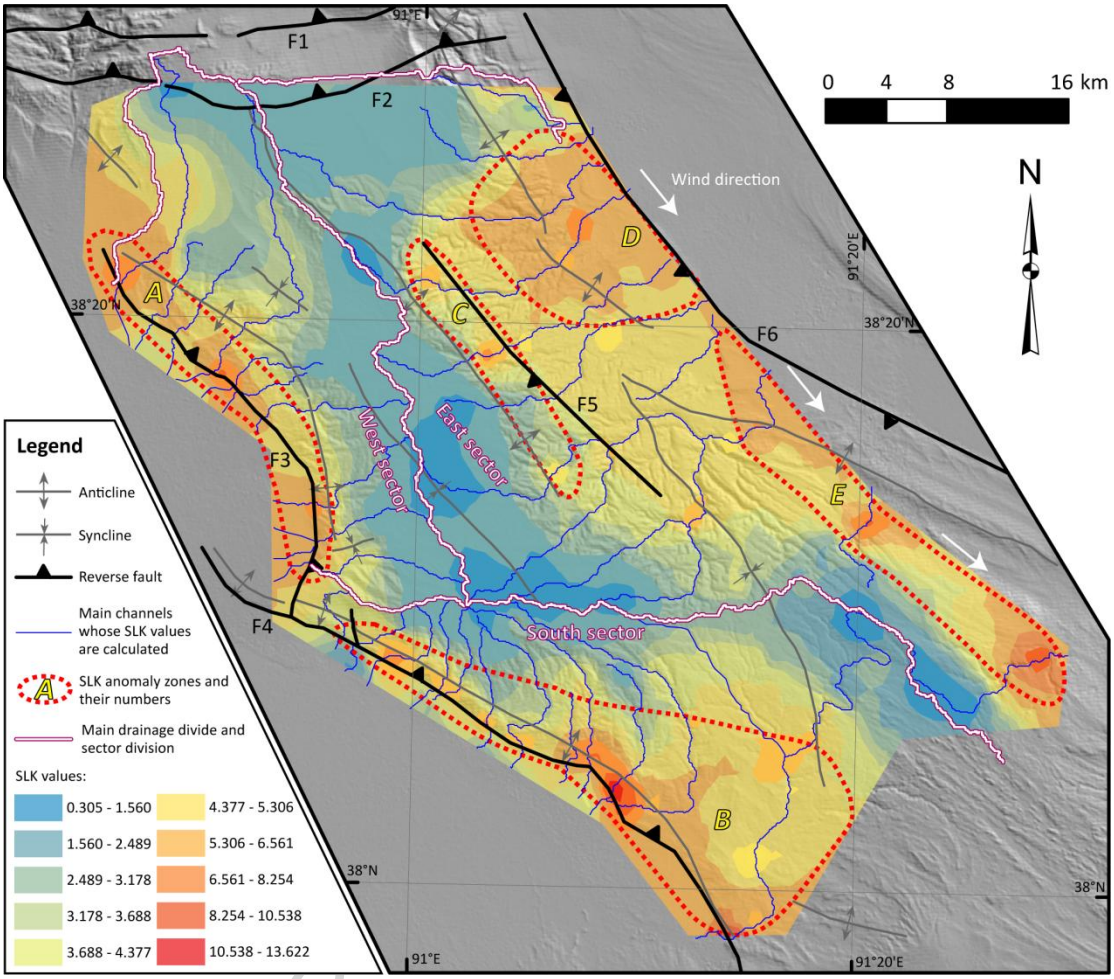

Fig. 10

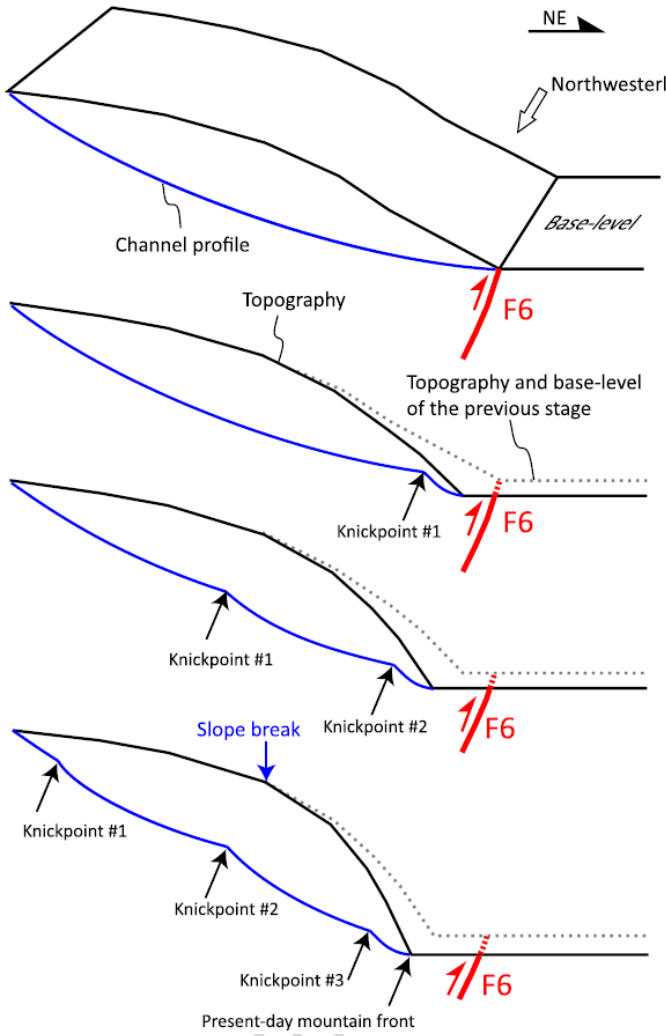

Stage 1: Equilibrium channel before initiation of wind erosion

Stage 2: Winds lowered the base-level and eroded the mountain-front laterally, generating a knickpoint (#1) close to the outlet of the channel

Stage 3: Continuous base-level lowering and lateral erosion steepened the mountain front and produced the second knickpoint (#2). Note that the knickpoint #1 was reteating towards the upstream

Stage 4: Same as Stage 3. New knickpoint (#3) was formed. The old knickpoints #1 and #2 were continuously reteating upstream, resulting in the increase of channel incision (or topographic relief). Continuous lateral erosion resulted in a steep mountain front with an obvious slope break

Fig. 11

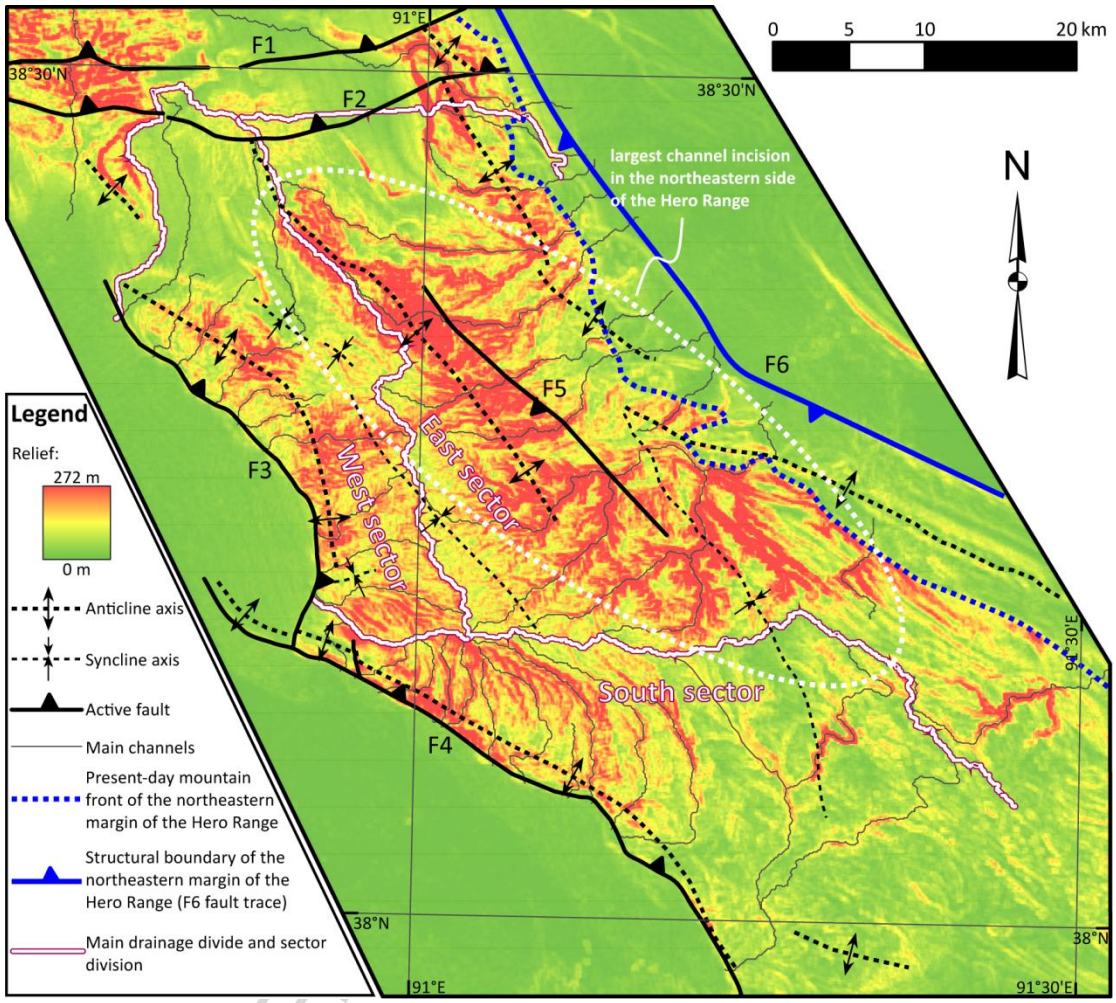

Fig. 12

Table 1 Summary of the active tectonics in the Hero Range determined from geological evidences and geomorphic indexes, and their consistency *

	West sector	**South sector**	**Western part**	
Type of erosion	Fluvial incision	Fluvial incision	Fluvial incision	
		Geological evidences		
Geological features	Shizigou anticline and Shizigou fault (F3)	Youshashan anticline and Youshashan fault (F4)	Ganchaigou anticline and Gandong fault (F5)	X anticl
Fault traces	3	3	2	
Fault scarps	3	3	/	
Faulted Holocene fans	/	3	/	
Seismicity	2	3	2	
Channel merging and bending	/	/	2	
Geological activity index	2.67	3	2	
Activity	Strongly active	Strongly active	Moderately active	W
		Geomorphic indexes		
Channels and catchments	#1 - 8	#9 - 18	Upstream of #21 – 25	downs
Hypsometric curves	2	2	/	
Longitudinal channel profiles (knickpoints)	3	3	2	
SLK	3	3	2	
Geomorphic activity index	2.67	2.67	2	
Activity	Strongly active	Strongly active	Moderately active	Mo
Consistency	Yes	Yes	Yes	

* The geological evidences and geomorphic indexes are quantified by values of 1, 2 and 3 indicating weakly, moderately and strongly active tectonics, respectively. The geological and geomorphic activity indexes are mean values of corresponding evidences or indexes, with values of >2.5, 1.5 – 2.5 and < 1.5 as indicators of strong, moderate, and weak activity, respectively. "/" means no data.

Highlights

1. The impact of wind erosion on geomorphic indexes is evaluated
2. The case study was developed on Hero Range in the western Qaidam Basin
3. Wind erosion makes geomorphic indexes showing higher activities
4. Wind erosion affects the indexes by base-level lowering and lateral erosion